Journal of Power Sources 195 (2010) 5692–5706

Contents lists available at ScienceDirect

Journal of Power Sources

journal homepage: www.elsevier.com/locate/jpowsour

Constitutive modeling of the rate, temperature, and hydration dependent deformation response of Nafion to monotonic and cyclic loading

Meredith N. Silberstein, Mary C. Boyce*

MIT, Department of Mechanical Engineering, 77 Massachusetts Avenue, Cambridge, MA 02139, United States

ARTICLE INFO

Article history:
Received 2 February 2010
Received in revised form 11 March 2010
Accepted 12 March 2010
Available online 20 March 2010

Keywords:
Polymer mechanics
Nafion
PEM fuel cells
PFSA membranes
Hygrothermal coupling
Micromechanical modeling

ABSTRACT

The elastic–plastic behavior of the polymer electrolyte membrane (PEM) Nafion is characterized via monotonic and cyclic uniaxial tension testing as a function of strain rate, temperature, and hydration. Dynamic mechanical analysis shows that, under dry (30%RH) conditions, the material begins to transition from the glassy to the rubbery state at 75 °C, with a glass transition of 105 °C. DMA reveals the fully hydrated state to be significantly more compliant than the dry state, with a glass transition beginning at 40 °C. Large strain monotonic tensile tests find the rate-dependent stress–strain behavior to be highly dependent on temperature and hydration. The dry state transitions from an elastic–plastic behavior at 25 ° C to an increasingly more compliant behavior and lower yield stress as temperature is increased through the glass transition, until exhibiting a rubbery-like behavior at 100 °C. At 25 °C, the stress–strain behavior remains elastic-plastic for all hydrated states with the stiffness and yield stress decreasing with increasing hydration. Increasing hydration at all temperatures acts to decrease the initial elastic stiffness and yield stress. Unloading from different strains reveals the elastic-plastic nature of the behavior even for the elevated temperature and hydrated states. Cyclic loading-unloading-reloading excursions to different strains show significant nonlinear recovery at all strains past yield with a highly nonlinear reloading behavior which rejoins the initial loading path. A micromechanically motivated constitutive model consisting of an intermolecular resistance in parallel with an elastic network resistance is shown to be capable of capturing the rate, temperature, and hydration dependence of the monotonic stress-strain behavior. The intermolecular resistance captures the local intermolecular barriers to initial elastic deformation and also captures the thermally activated nature of yield; these intermolecular barriers are modeled to decrease with increasing temperature and hydration, in particular mimicking the reduction in these barriers as the material approaches and enters the glass transition regime, successfully capturing the strong temperature and hydration dependence of the stress-strain behavior. The highly nonlinear post-yield unloading and reloading suggest the development of a back stress during inelastic deformation which aids reverse plastic flow during unloading. Inclusion of a back stress which saturates after reaching a critical level provides an ability to capture the highly nonlinear cyclic loading stress response. Hence, the proposed model provides the capability to describe the complex evolution of stress and strain that occurs in PEM membranes due to the constrained hygrothermal cyclic swelling/deswelling characteristic of membranes in operating fuel cells.

1. Background

Polymer electrolyte membranes provide a mechanically stable form of electrolyte and are utilized in a growing number of applications including fuel cells, batteries, and solar cells. These materials typically have covalently bonded ionizable groups which result in interesting chemical and electro-active properties which also influences the mechanical behavior. A prominent application is the proton exchange membrane fuel cell (PEMFC) which converts chemical to electrical energy. The current usefulness of PEMFC technology is limited by the lifespan and the high cost of the fuel cell unit. The membrane electrode assembly (MEA), which consists of a selectively permeable polymer electrolyte membrane with a catalyst layer and porous carbon electrode support on each side, is a major factor in the unit lifespan and cost. The cyclic operating conditions of automobiles lead to MEA failure as characterized by the development of pinholes which then allow crossover of hydrogen and oxygen [1]. The cause of pinhole formation is a subject of debate, but one of the leading theories is that it is related to

* Corresponding author at: MIT, Department of Mechanical Engineering, Rom 3-173, 77 Massachusetts Avenue, Cambridge, MA 02139, United States.
Tel.: +1 617 253 2342; fax: +1 617 258 8742.
E-mail addresses: meri.silberstein@gmail.com (M.N. Silberstein), mcboyce@mit.edu (M.C. Boyce).

0378-7753/$ – see front matter © 2010 Elsevier B.V. All rights reserved.
doi:10.1016/j.jpowsour.2010.03.047

mechanical stress in the membrane due to hygrothermal cycling. Hence, the mechanical behavior of polymer electrolyte membranes and its dependence on temperature and hydration is of interest for the design of robust PEMFCs.

The persulfonated polytetrafluoroethylene membrane Nafion is perhaps the most commercially prominent and widely studied membrane. The mechanical behavior has been a subject of investigation in recent years (e.g. Kundu et al. [1], Tang et. al. [2], Satterfield et. al. [3], Majsztrik et. al. [4], Satterfield and Benziger [5], Liu et al. [6], Liu et al. [7], and Kusoglu et al. [8]). Collectively, through various experiments including DMA, monotonic tensile, stress relaxation, and creep these studies have identified the dependence of the modulus, yield stress, and post-yield behavior on rate, temperature, and hydration level. The elastic modulus and yield stress were found to decrease significantly with increasing temperature and hydration and to increase slightly with increasing strain rate.

On the modeling front, Weber and Newman [9] were the first to incorporate mechanical properties into a Nafion model for fuel cell applications. Their one-dimensional model included conductivity, water transport, swelling, and the hydrostatic mechanical behavior of Nafion. This model demonstrated the importance of mechanical constraints on the membrane water content and electrochemical performance. Tang et al. [2] modeled the membrane behavior as isotropic linear-elastic with isotropic thermal and hydration expansion, where the elastic and expansion properties were taken as constants independent of temperature and hydration. Kusoglu et al. [10] expanded this model to include yielding assuming elastic-perfectly-plastic behavior and included more detailed characterizations of the thermal and hydration expansion behaviors. Both the elastic modulus and yield stress were given as functions of temperature and relative humidity based on experimental data from Tang et al. [2]. Kusoglu et al. [11] further improved the model, fitting experimental data to a phenomenological model to capture the temperature and relative humidity dependence of the stress–strain behavior under constant strain rate monotonic loading. Recently these authors have shown that when Nafion is submerged in water it is more appropriate to model it as a rubber rather than as a semicrystalline polymer [8]. Solasi et al. [12] used a constitutive model consisting of two dissipative mechanisms to capture the nonlinear time dependent hygrothermomechanical behavior. The model was able to simulate monotonic uniaxial tension with hydration and strain rate-dependent yield, moderate strain hardening, and stress relaxation at low to moderate strains. Lai et al. modeled Nafion as linear viscoelastic with linear expansions in temperature and water content, using relaxation master curves to account for shifts due to temperature and hydration [13]. In situ simulations that were performed with this model suggest that a model which incorporates the viscoplastic nature of Nafion is required.

Given that the critical loading conditions of a fuel cell membrane arise due to cyclic temperature and hydration conditions under constrained conditions, the aim of this paper is to develop a model that captures the rate, temperature, and hydration dependent elastic–plastic stress–strain behavior during monotonic and cyclic (load–unload–reload) loading conditions. The mechanics of such constrained conditions result in significant stresses in the plane of the membrane as further supported by simulations of the in situ fuel cell membrane [10,14] underlying the importance of the in-plane mechanical behavior of the membrane. Hence, the experimental portion of this study explores and quantifies the effect of temperature and hydration (via liquid water rather than relative humidity) on the uniaxial tensile stress–strain response of Nafion NRE212 under monotonic and cyclic loading profiles. This comprehensive data set is then used to develop a microstructurally motivated three-dimensional constitutive model. Constitutive model results are then compared to the experimental data, identifying which key elements of the model govern the important features and dependencies of the stress–strain behavior.

2. Experiments: methods

2.1. Materials

Commercially available dispersion cast NRE212 films (thickness $t = 54\mu m$, Dupont, Ion Power Inc.) were used for the experimental characterization of Nafion. The films were stored in a desiccator cabinet upon removal from the initial packaging to minimize variability in data from aging and humidity effects. The material was tested either as-received or after a chemical pre-treatment commonly used to purify and acidify the membrane in experimental fuel cell systems.

The pre-treatment entailed soaking the membrane in hydrogen peroxide (H_2O_2) for 1 h at 85 °C to remove any impurities, soaking in deionized water for 1 h at 85 °C to rinse the hydrogen peroxide, soaking in sulfuric acid (H_2SO_4) for 1 h at 85 °C to fully acidify the membrane, and finally soaking in deionized water at 80 °C for an additional hour to rinse away the excess sulfuric acid. The pre-treated specimens were dried in a desiccator cabinet for at least 24 h prior to testing.

2.2. Dynamic mechanical analysis

Dynamic mechanical analysis (DMA) testing was performed on a TA Instruments Q800 Dynamic mechanical analyzer. Specimens were cut 5 mm wide with a set of parallel blades. The specimens were positioned in the grips to have a gauge length of approximately 10 mm and were tested in uniaxial tension at a frequency of 1 Hz and amplitude of 15 μm. The temperature was increased from −10 °C to 170 °C at a heating rate of 3 °C per minute. Tests were also conducted on specimens submerged in deionized water. For these tests the temperature was increased from 10 °C to 80 °C at 1 °C per minute as this is the temperature limit imposed by the device. For consistency the submerged specimens are compared to "in air" specimens undergoing the same temperature sweep.

2.3. Tensile testing

Uniaxial tension tests were conducted at constant engineering strain rates from $0.001\,s^{-1}$ to $0.1\,s^{-1}$, at temperatures from 25 °C to 100 °C, and at various water contents. The film was cut into tensile specimens using a dogbone shaped die with gauge length of either 9.54 mm or 4.0 mm and gauge width of 3.14 mm. The nominal thickness is 54 μm. The thickness of each specimen was determined from the average of three measurements taken along the gauge length with a Mitutoyo micrometer. All tensile tests were conducted on an EnduraTEC Electroforce 3200 (ELF). All tests were conducted in displacement control mode. The maximum strain achieved in each trial is limited by the 12 mm stroke length of the ELF. Strain was measured with a Qimagine Retiga 1300 video extensometer. The force–displacement data as taken from the ELF and the videoextensometer, respectively, were reduced to true stress–true strain results assuming isotropic incompressible behavior. True stress is defined as the ratio of force to current (deformed) cross-sectional area and true strain is defined as the natural logarithm of the ratio of current length to original length (length being the axial distance between video-imaged marks). For completeness, specimens were tested in multiple directions and the membrane was found to be isotropic in the plane [15]; hence, results will be presented for one direction only.

Temperatures above room temperature were achieved using a Sun Systems ET1 Environmental Chamber. The specimens were allowed to equilibrate at temperature for 30 min prior to testing.

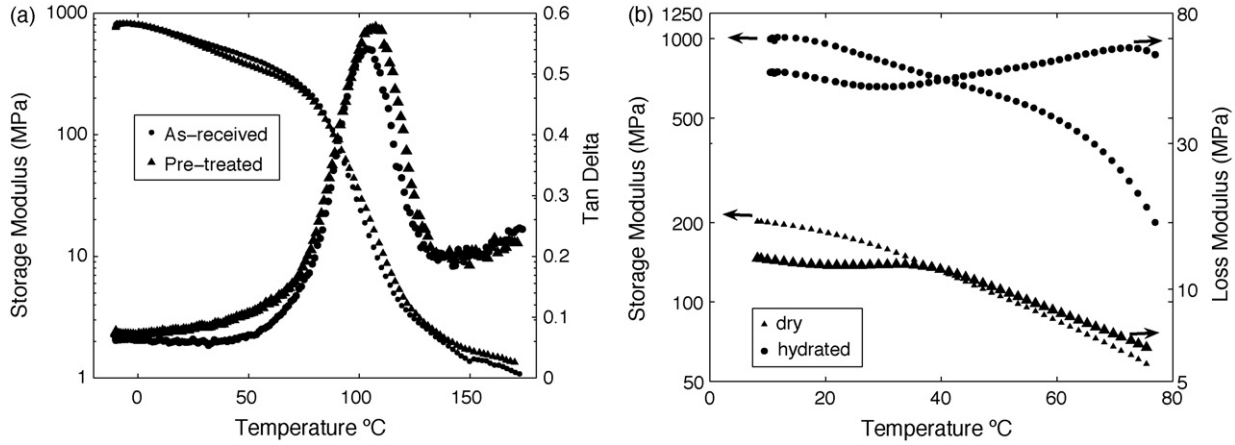

Fig. 1. (a) Storage modulus and loss factor as a function of temperature for as-received and pre-treated NRE212, conducted at 1 Hz. (b) Storage modulus and loss modulus as a function of temperature for dry and hydrated as-received NRE212, conducted at 1 Hz.

Hydration tests were conducted either "in air" or while immersed in water. For the "in air" tests, the specimens were imaged when dry, then submerged in deionized water for at least 30 min, removed from the water for a variable amount of time in accordance with desired water content, and then placed in the tensile grips and tested immediately. The "water immersed" tests were conducted in a custom built water chamber fitted to the ELF. The specimen was mounted in the grips and imaged. Water was then added to completely submerge the specimen. The top grip was raised until the specimen reached a zero-stress position at which point the tension test was conducted. For both types of hydration tests, the swelling percentage was calculated from the change in the distance between dots marked on the specimen from the dry state to the hydrated state at the start of the test; this change was found using video extensometer images and was calculated as the average of at least five pairs of dots. The standard deviation of the swelling calculation was typically 20% of the calculated value. Stress was calculated from the swollen cross section assuming through-thickness swelling to be equal to in-plane swelling. The stress may therefore be overestimated by roughly 5% if the through-thickness swelling is indeed greater than the in-plane swelling as suggested by studies on other forms of Nafion [16,17]. This linear swelling measurement can be converted to an approximation of the mole ratio, ϕ, of water to sulfonic acid groups assuming additive volumes and an initial value of 1.5 at ambient conditions (25 °C, 30%RH) [18]. $\phi = 31[(\lambda^s + 0.016)^3 - 1]$ where λ^s is the swelling stretch (derivation in Appendix A).

Hydration tests at elevated temperatures were conducted by heating the water prior to pouring it into the water chamber. The procedure was otherwise identical to that for a "water immersed" test.

3. Experiments: results and discussion

3.1. Dynamic mechanical analysis

The storage modulus, E', and loss factor (tan delta) from DMA testing of Nafion "in air" showed a broad transition temperature regime (Fig. 1a). While the peak of the tan delta curve occurs at 105 °C, the storage modulus begins to drop noticeably as early as 20 ° C with a steep drop beginning at approximately 70 °C. There is no marked change in the storage or loss curves or glass transition due to the chemical pre-treatment. This peak location is in agreement with previous studies including the seminal paper of Yeo and Eisenberg and is considered the glass transition temperature of Nafion [18]. Hydration is seen to dramatically reduce the storage and loss modulus at all temperatures (Fig. 1b). The storage modulus for 25 ° C and hydrated is the same as that for 80 ° C and dry. The glass transition in the hydrated data is hard to identify due to the limited temperature range; taking the point where the loss modulus begins to drop; the start of the glass transition region has shifted to a lower temperature of ~40 ° C from around ~75 °C.

3.2. Tensile testing

The uniaxial tensile behavior of Nafion during loading at 25 °C, as shown in Fig. 2, is characterized by a small linear-elastic region at strains less than about 0.02 followed by a gradual rollover yield occurring over a strain ranging from approximately 0.05 to 0.11. Post-yield strain hardening is then observed with the strain hardening slope increasing slightly with increasing strain. The unloading behavior after a strain of 0.60 is initially linear, it then transitions to a nonlinear recovery prior to reaching zero-stress, resulting in an initial unloaded strain of 0.47. Further recovery occurs during the time when the grip displacement is still changing (the grips are programmed to return to their original position and then to separate again to give the reloading; the thin flexible specimen elastically buckles during the unloading), and the specimen begins its reload from a strain of 0.40. The reload curve shows a shoulder at a stress

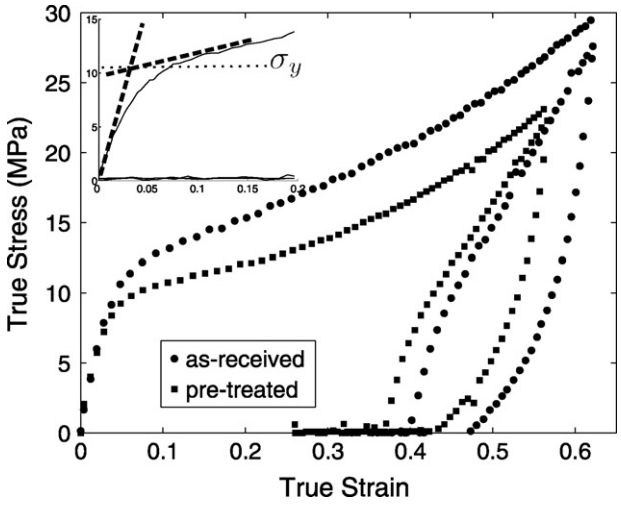

Fig. 2. Comparison of pre-treated and as-received material true stress–true strain behavior in uniaxial tension at 0.01 s^{-1} and 25 ° C (inset: yield stress definition).

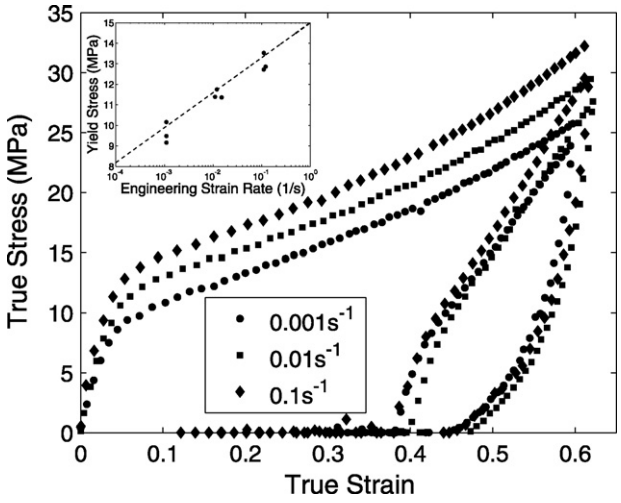

Fig. 3. True stress–true strain behavior at 25° C at multiple strain rates (inset: logarithmic rate dependence of yield stress).

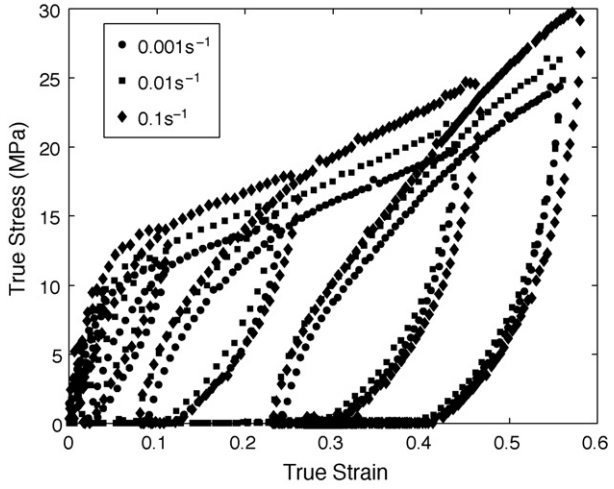

Fig. 4. True stress–true strain behavior under uniaxial tensile cyclic loading conditions at 25° C at multiple strain rates.

below that of the initial yield and essentially rejoins the initial loading curve when it reaches the maximum strain for the second time. The yield stress σ_y is take to be the stress at the intersection of linear fits to the initial elastic slope and the immediate post-yield strain hardening slope (Fig. 2).

The pre-treated material was shown to exhibit a slightly lower stiffness, yield stress, and subsequent post-yield stress, than that of the as-received material, but to have qualitatively the same behavior as the as-received material (Fig. 2). Additional results will be presented only for the as-received material, but the discussion also holds for behavior observed in the pre-treated material [15].

3.2.1. Strain rate dependence

The strain rate dependence of the stress–strain behavior at 25° C is shown in Fig. 3. There is a slight increase in the elastic modulus and a significant increase in the yield stress as the strain rate is increased. The yield stress has a logarithmic dependence on strain rate (Fig. 3 inset). The post-yield strain hardening slope is relatively insensitive to strain rate.

3.2.2. Cyclic loading

The viscoplastic behavior is further quantified in cyclic loading profiles. The stress–strain behavior during loading, unloading, and reloading to increasing strain values is shown in Fig. 4. The unloading behavior is characterized by a relatively stiff linear region which becomes increasingly more compliant as unloading progresses and the stress decreases; this behavior indicates the development of a significant back stress during loading which aids recovery during unloading, e.g. [19,20]. Further strain recovery occurs during the time period when the grip displacement is still returning to its initial position (while the specimen is essentially unloaded), leading to reloading curves beginning at a smaller strain than the strain immediately after unloading. Reloading is characterized by an initially stiff linear region with a rollover to a more compliant behavior. The reloading stiffness is lower than the initial stiffness. The reloading rollover yield stress level is substantially lower than the initial yield stress and is followed by a relatively steep post-yield slope until rejoining the initial loading curve. The reloading rollover yield stress is found to decrease with an increase in the applied strain, but tends toward a steady value. Fig. 4 shows the cyclic behavior at three different strain rates, exhibiting the expected rate dependence of these hysteresis loops.

3.2.3. Temperature and hydration dependence

The mechanical behavior has a strong dependence on temperature and hydration. Tests conducted at an engineering strain rate of 0.01 s^{-1} at temperatures from 25° C to 100° C are shown in Fig. 5a. In agreement with the trends observed on other forms of

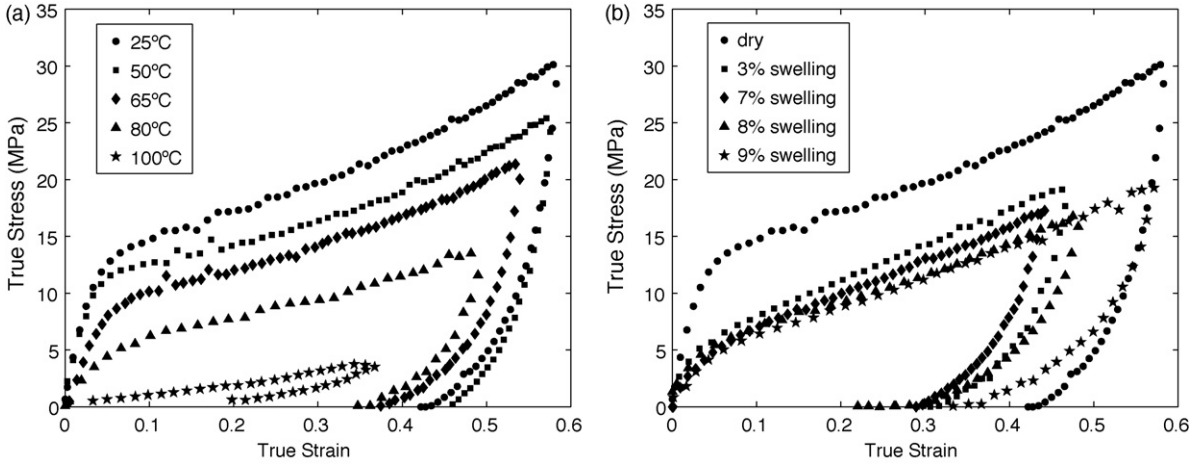

Fig. 5. True stress–true strain curve at 0.01 s^{-1} and (a) as a function of temperature; (b) as a function of hydration.

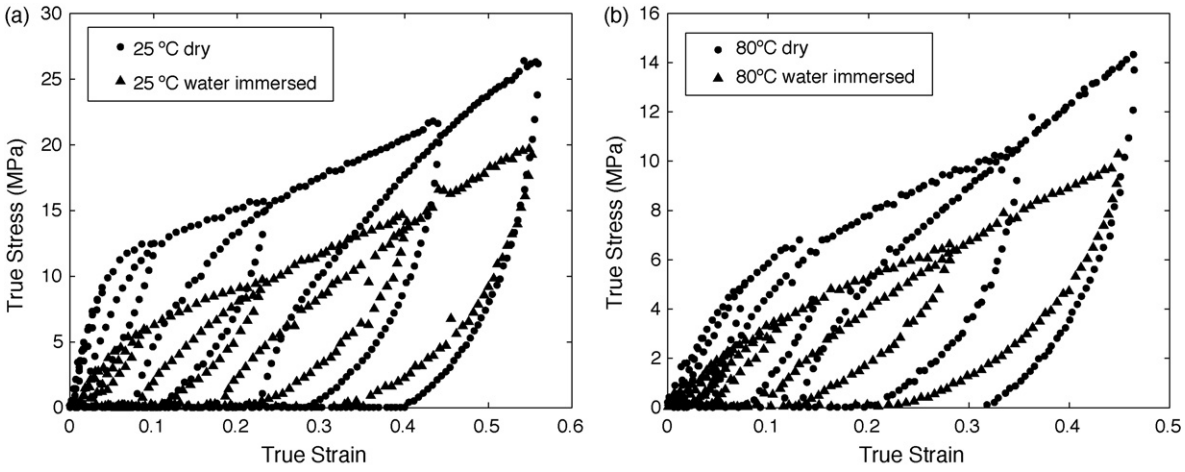

Fig. 6. True stress–true strain behavior under uniaxial tensile cyclic loading conditions at elevated temperature and hydration at a strain rate of 0.01 s^{-1} (a) 25 ° C and (b) 80 °C.

Nafion [2,3], there is a decrease in the initial elastic modulus and the yield stress, an increase in the yield strain, and a slight decrease in the post-yield tangent modulus when the temperature is increased. The yielding event tends more towards a rollover rather than a clear yield point as the temperature is increased.

The strong dependence of the mechanical behavior on hydration is shown in Figs. 5b and 6, in accordance with the observations of other investigations on other forms of Nafion [1–6]. The elastic modulus and yield stress decrease rapidly and then plateau as the water content is increased (Fig. 5b). Under cyclic loading the same characteristic hysteresis features are observed at elevated temperature and hydration as at dry 25 ° C conditions, albeit at lower stress levels (Fig. 6).

The yield stress dependence on temperature for both the dry and water immersed cases is summarized in Fig. 7. For the dry case, the yield stress shows a small temperature dependence from 20 ° C to 50 ° C and then a more dramatic decrease from 50 ° C to 100 °C; this decrease is consistent with the DMA data where the storage modulus decreases gradually at first and then has a sharp drop centered around 100 °C. As expected, at every temperature the yield stress for the hydrated specimen is lower than that for the dry specimen. These data also suggest that hydration shifts the glass transition regime to lower temperatures in agreement with the DMA data. These data are consistent with the water acting as a "plasticizer",

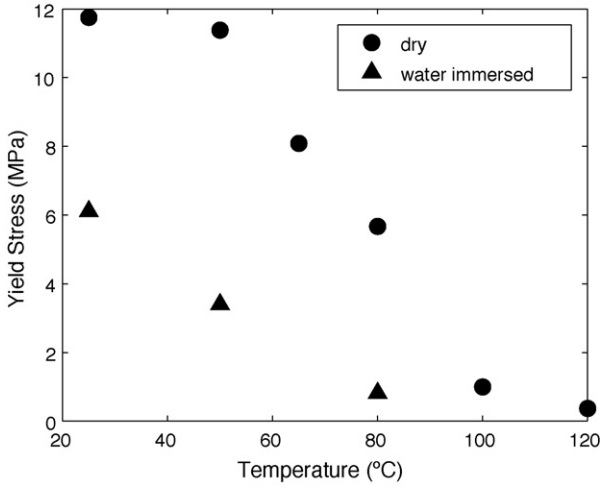

Fig. 7. Yield stress as a function of temperature at an engineering strain rate of 0.01 s^{-1}.

lowering the glass transition temperature as well as reducing the modulus and yield stress at all temperatures.

Based on the preceding experimental results an accurate and useful model for the loading scenarios encountered in fuel cell systems should capture:

- Initial elastic behavior.
- Rate-dependent distributed yield event.
- Strain hardening.
- Nonlinear unloading and reloading.
- Strain dependent reloading yield stress.
- Strain dependent reloading post-yield hardening behavior.
- Temperature and hydration dependence of all of the above, including transitioning from the glassy state at 25 °C, RH = 30% into the glass transition regime with increasing temperature and hydration.

4. Modeling

An elastic–viscoplastic constitutive model consisting of an intermolecular deformation mechanism acting in parallel with a molecular network alignment mechanism is adopted to capture the features of the mechanical behavior of Nafion discussed above. The model framework follows those presented for thermoplastics and time dependent elastomers in the prior work of Boyce and co-workers [21–27], Buckley and Jones [28], Bergstrom and Hilbert [29], and more recently adopted by Anand and co-workers [30,31]. First, a simplified version of the model (Model I) will be presented which is found to capture the monotonic loading behavior. Second, in order to capture the cyclic (unloading, reloading) behavior, additional sophistication will be added to the model (Model II).

4.1. Model I

A rheological schematic of the proposed Model I is shown in Fig. 8. A fundamental assumption in the model structure is that the stress response of a material can be decomposed into multiple mechanisms. In this case two mechanisms are needed to model the material behavior: Mechanism I, rheologically depicted as an elastic spring in series with a viscoplastic dashpot, represents the resistance to deformation due to the intermolecular interactions where the spring captures the stiffness of these interactions and the nonlinear dashpot captures the yielding of these interactions; Mechanism N is a nonlinear spring which represents a resistance due to the stretching and orientation of the molecular network.

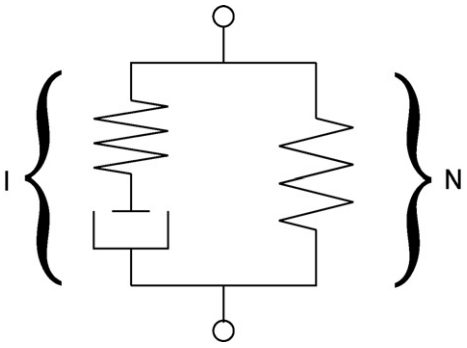

Fig. 8. Rheological representation of Model I: elastic–viscoplastic.

The intermolecular resistance (Mechanism I) is strongly dependent on temperature and hydration, it is important to note that intermolecular interactions decrease significantly when the polymer goes from the glassy state into the glass–rubber transition regime. The network resistance (Mechanism N) is operational at all temperatures.

The model is fully three-dimensional but will be expressed in principal stretch space for simplicity. Throughout this discussion $i = 1, 2, 3$ are taken to indicate the three principal stretch directions with no sum on repeated i unless otherwise noted. The macroscopic deformation is given by the principal stretches λ_i. Each mechanism is taken to experience the same deformation and the total stress acting on the system is equal to the sum of the contributions from each mechanism:

$$\lambda_{Ii} = \lambda_{Ni} = \lambda_i \tag{1}$$

$$T_i = T_{Ii} + T_{Ni} \tag{2}$$

where λ_{Ii} and λ_{Ni} are the principal stretches of the intermolecular (I) and network (N) mechanisms, respectively, and T_{Ii} and T_{Ni} are the Cauchy (true) stress contributions of the intermolecular and network mechanisms, respectively.

4.1.1. Mechanism I

At 25 °C, the intermolecular mechanism provides the dominant resistance to deformation at small to moderate strains. The stretch λ_{Ii} is accommodated by both elastic deformation and plastic deformation as captured through the Kroner–Lee decomposition $\lambda_{Ii} = \lambda^e_{Ii}\lambda^p_{Ii}$, where λ^e_{Ii} are the elastic stretches and λ^p_{Ii} are the plastic stretches. The plastic deformation is assumed isochoric such that the plastic volume ratio $J^p = \lambda^p_1\lambda^p_2\lambda^p_3 = 1$. The corresponding rate kinematics are described by the velocity gradient $D_{Ii} = \dot{\lambda}_{Ii}\lambda_{Ii}^{-1}$, which can be decomposed into elastic and plastic contributions:

$$D_{Ii} = D^e_{Ii} + D^p_{Ii} \tag{3}$$

where $D^e_{Ii} = \dot{\lambda}^e_{Ii}(\lambda_{Ii}{}^e)^{-1}$ is the elastic velocity gradient and $D^p_{Ii} = \dot{\lambda}^p_{Ii}(\lambda_{Ii}{}^p)^{-1}$ is the plastic velocity gradient. D^p_{Ii} will be constitutively prescribed later.

The intermolecular contribution to the Cauchy stress is taken to be a function of the elastic stretches:

$$T_{Ii} = \frac{1}{J^e}[2\mu(\ln\lambda^e_{Ii})' + \kappa \ln J^e] \tag{4}$$

where $J^e = \lambda^e_{I1}\lambda^e_{I2}\lambda^e_{I3}$ is the elastic mechanical volume ratio, μ is the shear modulus, and κ is the bulk modulus.

The plastic velocity gradient is constitutively prescribed to follow a thermally activated process driven by the stress deviator (note that we neglect linear viscous contributions since these were measured to be small compared to nonlinear viscous contributions):

$$D^p_{Ii} = \dot{\gamma}^p_I \frac{T'_{Ii}}{\sqrt{2}\tau_I} \tag{5}$$

$$\dot{\gamma}^p_I = \dot{\gamma}^o \exp\left[\frac{-\Delta G}{k_b\theta}\right] \sinh\left[\frac{\Delta G}{k_b\theta}\frac{\tau_I}{s}\right] \tag{6}$$

where $\dot{\gamma}^p_I$ is the magnitude of the plastic velocity gradient, $T'_{Ii} = T_{Ii} - (1/3)(T_{I1} + T_{I2} + T_{I3})$ is the stress deviator, $\tau_I = \sqrt{(1/2)(T'_{I1}{}^2 + T'_{I2}{}^2 + T'_{I3}{}^2)}$ is the scalar equivalent shear stress, $\dot{\gamma}^o$ is a pre-exponential factor proportional to the attempt frequency, ΔG is the activation energy, s is the isotropic shear resistance, k_b is Boltzmann's constant, and θ is the absolute temperature.

A constant value for the shear resistance s would give a sharp transition from elastic to plastic behavior. The inhomogeneous nature of the Nafion microstructure makes this physically unrealistic, as is evident in the gradual yielding observed in the stress–strain curves. The distributed microstructure provides a spatial distribution in the strength of interactions which in turn corresponds to progressively activating plastic deformation at different levels of stress. At a critical stress, the site with the lowest resistance to shear will begin to deform plastically while the rest of the material will continue to deform elastically. The plastically deforming sites harden slightly which, in turn, raises the overall stress level, activating deformation of higher strength sites. As more sites reach their respective critical stress state, plasticity percolates and the material behavior will macroscopically roll over from elastic to plastic behavior. Rheologically this would be represented as an infinite number of spring-dashpot pairs in parallel, however, it is much simpler to capture this effect mathematically as an evolution in shear resistance s. Hence, the initial shear resistance $\tilde{s}_o$ is taken to increase with $\dot{\gamma}^p_I$ until reaching a saturated state $\tilde{s}$ during plastic deformation:

$$\dot{\tilde{s}} = \tilde{h}\left(1 - \frac{\tilde{s}}{\tilde{s}_{sat}}\right)\dot{\gamma}^p_I \tag{7}$$

where $\tilde{h}$ controls the approach of $\tilde{s}$ to $\tilde{s}_{sat}$ with plastic strain. Molecular alignment provides an additional increase to the intermolecular shear resistance captured by the contribution $\bar{s}$:

$$\bar{s} = \bar{h}(\lambda^{\bar{n}}_{chain} - 1) \tag{8}$$

where $\bar{h}$ controls the initial slope, $\bar{n}$ controls the nonlinearity, and $\lambda_{chain} = \sqrt{(\lambda_1^2 + \lambda_2^2 + \lambda_3^2)/3}$ is a measure of network stretch. The shear resistance (s) is then given by:

$$s = \tilde{s} + \bar{s}. \tag{9}$$

The plastic deformation gradient can then be updated by integrating $\dot{\lambda}^p_{Ii} = D^p_{Ii}\lambda^p_{Ii}$ with time; the elastic stretch is calculated via $\lambda^e_{Ii} = \lambda_{Ii}\left(\lambda^p_{Ii}\right)^{-1}$.

4.1.2. Mechanism N

The stress arising from the network resistance to deformation (T_{Ni}) is taken to be deviatoric and is derived from the resistance to stretching and orientation of the molecular network; here we use the Neo–Hookean model:

$$T_{Ni} = \frac{1}{J}\mu_N B'_{Ni} \tag{10}$$

where $J = \lambda_1\lambda_2\lambda_3$ is the volume ratio, μ_N is the rubbery shear modulus, and B'_{Ni} is the deviatoric part of the Cauchy Green tensor given by $B'_{Ni} = \lambda^2_{Ni} - \lambda^2_{chain}$.

Temperature and hydration influence both the kinematics (due to the volumetric expansion associated with changes in temperature and water content) and the resistances to deformation, having a strong effect on the intermolecular interactions. Kinematically,

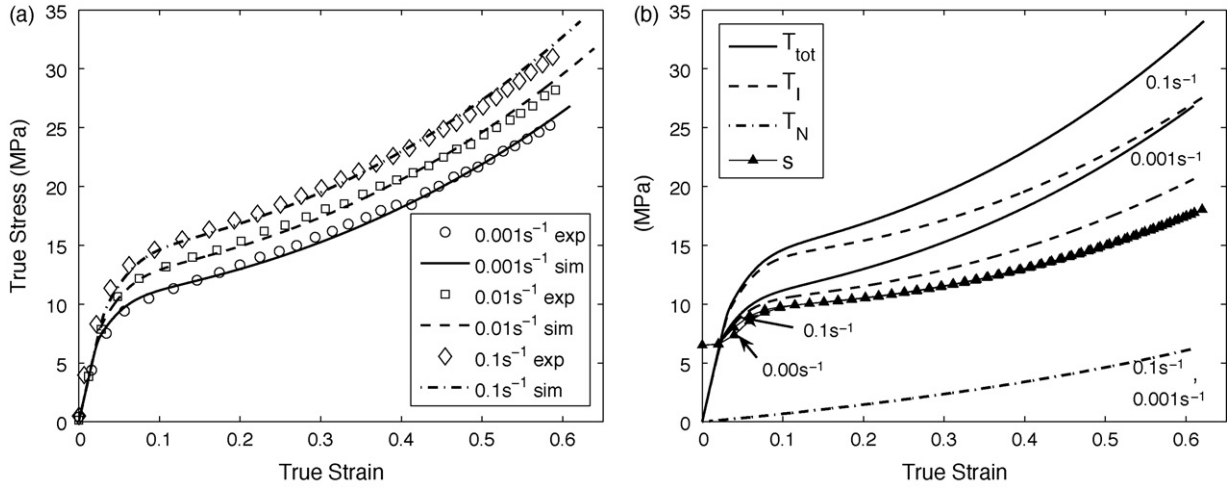

Fig. 9. Model I in uniaxial extension at ambient conditions at three different strain rates (a) comparison with experiments and (b) contributions of the individual mechanisms to the overall response.

the total principal intermolecular stretches can be decomposed into mechanical and swelling contributions as

$$\lambda_{Ii} = \lambda^e_{Ii}\lambda^p_{Ii}\lambda^s_{Ii} \tag{11}$$

where $\lambda^s_{Ii} = \lambda^s\left(1 + \beta\Delta\phi + \alpha\Delta\theta\right)$ is the deformation due hygrothermal-swelling, $\beta = (\partial \ln \lambda^s_{Ii}/\partial\phi)$ is the coefficient of hygro expansion, $\alpha = (\partial \ln \lambda^s_{Ii}/\partial\theta)$ is the coefficient of thermal expansion, $\Delta\phi$ and $\Delta\theta$ are the changes in ϕ and θ respectively relative to a reference state at which the model is calibrated (here chosen as 25 °C, 30%RH). We have assumed the hygro-swelling and thermal-swelling to be isotropic, linear, and uncoupled from each other and from the plastic deformation, but these can be generalized to depend on temperature and hydration and may be coupled. While there is some evidence that through-thickness swelling can be larger than in-plane swelling for some Nafion materials [13], we neglect that possible effect here since this model will be applied primarily to in-plane loading. As an aside we note that a multiplicative decomposition of the deformation gradient into swelled and mechanical contributions was utilized by Flory [32] for swelling rubber elastic materials as reviewed in Boyce and Arruda [33]. Here we have the additional complexity of inelastic deformation and also changes in temperature.

The rate kinematics are described by the velocity gradient, which can be decomposed into elastic, plastic, and hygrothermal-swelling contributions:

$$D_{Ii} = D^e_{Ii} + D^p_{Ii} + D^s_{Ii} \tag{12}$$

where $D^s_{Ii} = \dot{\lambda}^s_{Ii}(\lambda^s_{Ii})^{-1}$ is the hygrothermal-swelling velocity gradient. D^p_{Ii} is constitutively prescribed as before.

The shear modulus (μ) and the plasticity dependent portion of the shear resistance to plastic flow ($\tilde{s}$) are defined as functions of temperature and hydration deduced from the dependencies of the elastic modulus as a function of temperature and hydration; these dependencies closely mirror those of the shear storage modulus and those of the yield stress (see Appendix A). Temperature is given in absolute temperature or Kelvin. Hydration is given in moles of water per mole of sulfonic acid group in the membrane. As a first approximation the effect of temperature and hydration are taken to be uncoupled and multiplicative; this multiplicative factor will be referred to as the reduction factor. The current state values of μ and $\tilde{s}$, independent of temperature and hydration, are multiplied by this corrective reduction factor to obtain $\mu(\theta, \phi)$ and $\tilde{s}(\theta, \phi)$, respectively.

The network stretch can be decomposed into mechanical and swelling contributions as:

$$\lambda_{Ni} = \lambda^m_{Ni}\lambda^s_{Ni} \tag{13}$$

where λ^m_{Ni} are the network mechanical stretches and $\lambda^s_{Ni} = \lambda^s_{Ii}$ is the hygrothermal-swelling. The network mechanical deformation is calculated as $\lambda^m_{Ni} = \lambda_{Ni}\lambda^{s\,-1}_{Ni}$ for a known temperature and water content.

The swelling decreases the network crosslink density thereby decreasing the mechanical stiffness. The hydration dependent network response is therefore constitutively prescribed by

$$T_{Ni} = \frac{\mu_N}{J^m_N \lambda^s} B^{m\prime}_{Ni} \tag{14}$$

where $J^m_N = \lambda^m_{N1}\lambda^m_{N2}\lambda^m_{N3}$ is the mechanical volume ratio, μ_N the rubbery shear modulus is not a function of temperature or hydration, and $B^{m\prime}_{Ni}$ is the deviatoric part of the mechanical Cauchy Green tensor given by $B^{m\prime}_{Ni} = \lambda^{m\,2}_{Ni} - \lambda^{m}_{chain}{}^{2}$.

A method for reducing material properties is provided in Appendix A along with the parameter values; this method decomposes the stress–strain curve into contributions associated with the various components of the model which helps provide a more systematic fitting of the material properties.

4.1.3. Results: strain and strain rate

This relatively simple elastic–viscoplastic model is able to capture the linear-elastic response, the rate-dependent distributed yield event, and the nonlinear strain hardening (Fig. 9a). Various key contributions to the model stress–strain curve are shown in Fig. 9b. The initial elastic response is dominated by the intermolecular contribution since the network stiffness is much lower than the intermolecular stiffness. The intermolecular contribution to stress is seen to govern the rate-dependent yield with the distributed rollover yield following the shape of the evolution in s. The post-yield strain hardening results in part from the network stiffness (which is an anisotropic contribution) and in part from the evolution in s (which is an isotropic contribution).

4.1.4. Temperature and hydration

The model is compared to experimental data as a function of temperature and hydration in Fig. 10. The model is able to capture

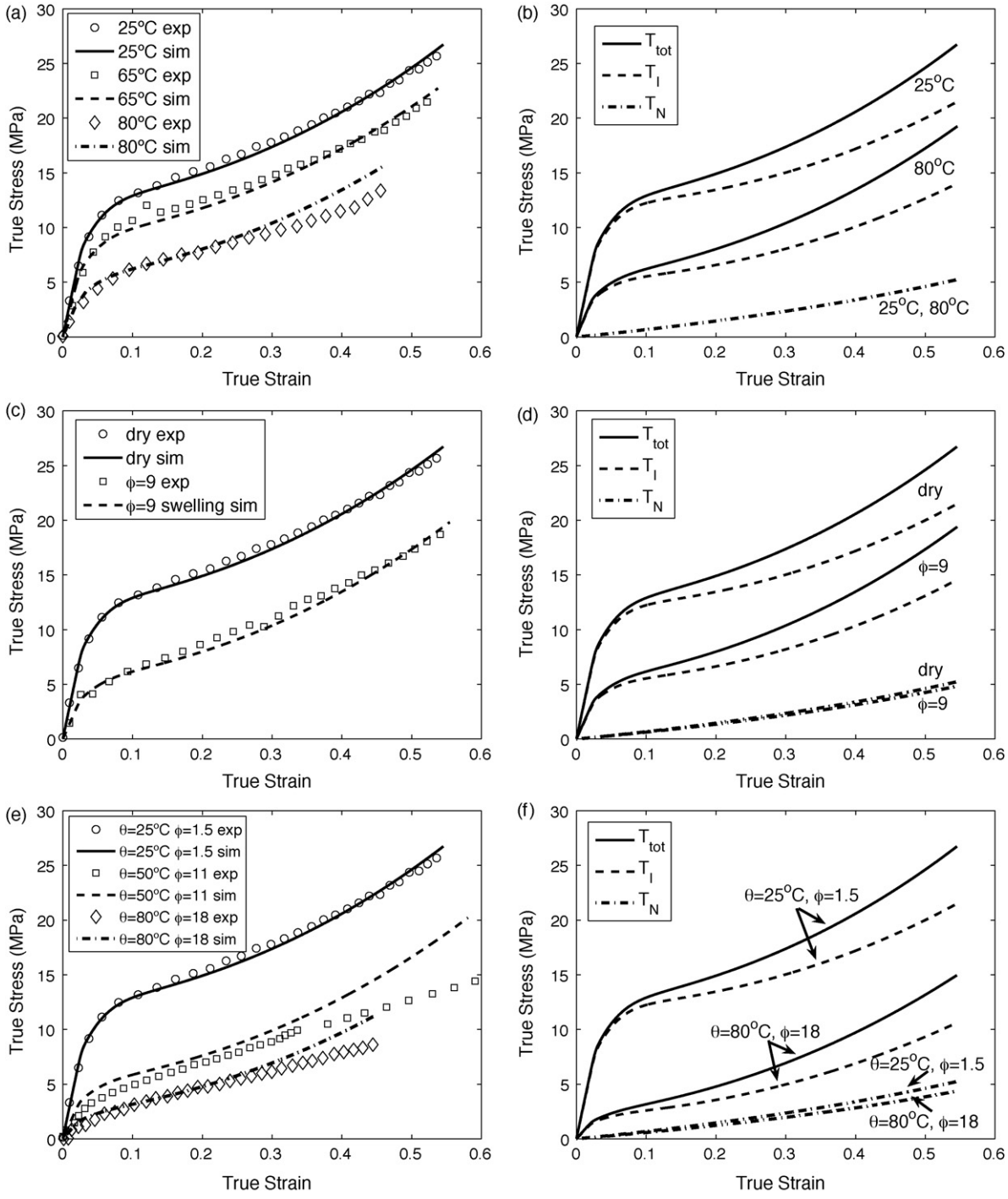

Fig. 10. Model I in uniaxial extension at a strain rate of 0.01 s^{-1} (a and b) at varied temperature (c and d) at varied hydration at 25 ◦ C (e and f) at varied hydration and temperature; (a, c, and e) comparison with experiments (b, d, and f) contributions of the individual mechanisms to the overall response.

the dependence of the elastic modulus and yield stress on temperature and hydration as well as the combined influence of changes in both temperature and hydration. This dependency is primarily in the intermolecular component; the network does not change at all with temperature (Fig. 10b) and changes only a small percentage with hydration (Fig. 10d and f).

4.1.5. Unloading and cyclic loading

Fig. 11 shows the model results including unloading and reloading from strains after yield. Clearly, Model I fails to capture the highly nonlinear unloading behavior. The unloading, reloading, and cyclic behavior is key to modeling membrane behavior in a functioning fuel cell due to the cyclic nature of fuel cell operation. This important effect is addressed next by including a back stress feature in Model II.

4.2. Model II

In order to address the inability of Model I to capture the cyclic behavior, a backstress component (B) is added to the intermolecular mechanism, as expressed rheologically in Fig. 12. It is assumed that during loading, due to the distributed heterogenous nature

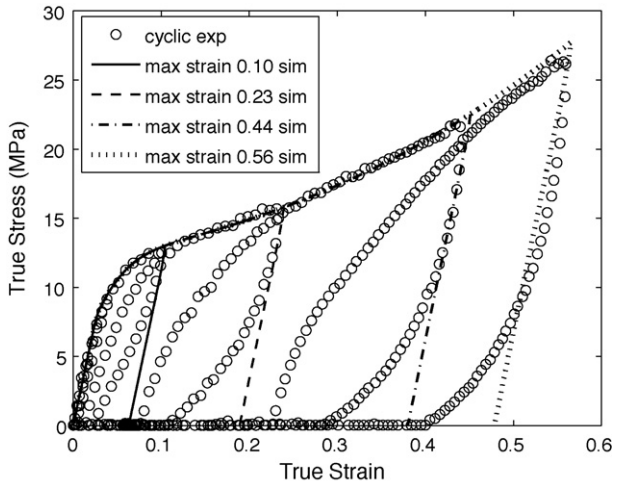

Fig. 11. Model I vs. experiment under tensile cyclic loading at a strain rate of 0.01 s^{-1} and ambient conditions showing the linear unloading behavior predicted by Model I in contrast to the nonlinear unloading that is experimentally observed.

of the Nafion microstructure, a back stress locally develops and is stored around plastically deforming regions. This back stress then assists reverse deformation during unloading. Calorimetric measurements [19,34] have indeed measured the development of such an energy storage mechanism during inelastic deformation of polymers. When the direction of loading is reversed, this back stress acts to assist inelastic deformation in the opposing direction and hence gives the nonlinear unloading response with a reverse yield. Here, the back stress is taken to evolve linearly with plastic deformation and to then saturate out as the plastically deformed regions percolate. The saturation is also observed in the calorimetry measurements [19,34]. The back stress saturation is captured by initiating a thermally activated plateau stress within a nonlinear viscous element physically governed by the same yielding mechanism as the intermolecular barrier. As indicated in the schematic of Fig. 12, the stretch acting on the back stress element is equal to that acting on the intermolecular viscoplastic dashpot ($\lambda_{Bi} = \lambda_{Ii}^{p}$). The back stress stretch can be decomposed into elastic and plastic components, $\lambda_{Bi} = \lambda_{Bi}^{e}\lambda_{Bi}^{p}$. The rate kinematics are given by $D_{Bi} = \dot{\lambda}_{Bi}\lambda_{Bi}^{-1}$, which can be further decomposed into elastic and plastic contributions:

$$D_{Bi} = D_{Bi}^{e} + D_{Bi}^{p} \tag{15}$$

where $D_{Bi}^{e} = \dot{\lambda}_{Bi}^{e}(\lambda_{Bi}^{e})^{-1}$ is the elastic velocity gradient and $D_{Bi}^{p} = \dot{\lambda}_{Bi}^{p}(\lambda_{Bi}^{p})^{-1}$ is the plastic velocity gradient which will be constitutively prescribed later.

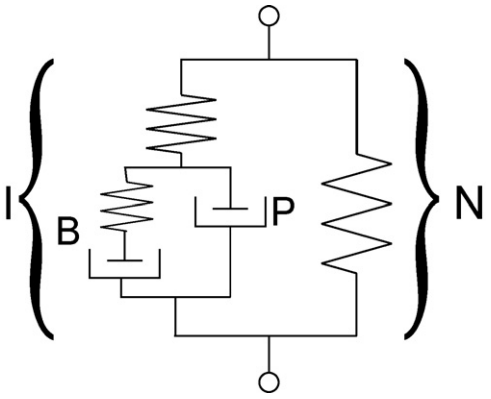

Fig. 12. Rheological representation of Model II: elastic–viscoplastic with back stress.

The elastic response of the back stress is given by:

$$T'_{Bi} = \frac{1}{J}2\mu_B \ln \lambda_{Bi} \tag{16}$$

where the back stress T'_{Bi} is naturally deviatoric since $\lambda_{B1}\lambda_{B2}\lambda_{B3} = 1$, μ_B is the back stress shear modulus.

The back stress velocity gradient is constitutively prescribed as:

$$D_{Bi}^{p} = \dot{\gamma}_B^{p}\frac{T'_{Bi}}{\sqrt{2}\tau_B} \tag{17}$$

$$\dot{\gamma}_B^{p} = \dot{\gamma}^{o}\exp\left[-\frac{\Delta G}{k_b\theta}\right]\sinh\left[\frac{\Delta G}{k_b\theta}\frac{\tau_B}{s_B}\right] \tag{18}$$

where $\tau_B = \sqrt{(1/2)(T'_{B1}{}^2 + T'_{B2}{}^2 + T'_{B3}{}^2)}$ is the corresponding equivalent shear stress and s_B is the isotropic shear resistance to inelastic deformation. $\dot{\gamma}^{o}$ and ΔG are the same constants as for the intermolecular plastic deformation since the rate dependence of unloading is similar to that of loading (Fig. 4). s_B is taken to evolve to a maximum with $\dot{\gamma}_B^{p}$ such that the saturation of the back stress occurs gradually:

$$\dot{s}_B = h_B\left(1 - \frac{s_B}{s_{Bsat}}\right)\dot{\gamma}_B^{p} \tag{19}$$

where h_B controls the evolution with shear and s_{Bsat} is the saturation value. λ_{Bi}^{p} can be updated by integrating $\dot{\lambda}_{Bi}^{p} = D_{Bi}^{p}\lambda_{Bi}^{p}$ with time; the elastic deformation gradient is then calculated via $\lambda_{Bi}^{e} = \lambda_{Bi}(\lambda_{Bi}^{p})^{-1}$.

The addition of a back stress as defined above does not alter the existing kinematics for Model I, but the constitutive definitions are modified slightly.

The cyclic experimental data show that the post-yield elastic unloading and reloading slopes are smaller than that of initial elastic loading; hence the shear modulus μ is taken to decrease with plastic strain to a minimum saturation state. This evolution reflects a rearrangement to a softened microstructure during the yielding process:

$$\dot{\mu} = h\left(1 - \frac{\mu}{\mu_{sat}}\right)\dot{\gamma}_I^{p} \tag{20}$$

where h controls the rate at which μ approaches the saturation value μ_{sat}.

The stress driving deformation of the intermolecular yield is now $[T_{Ii} - T_{Bi}]'$ and will be referred to as T'_{Pi}. Hence the expression for the plastic velocity gradient becomes:

$$D_{Ii}^{p} = \dot{\gamma}_I^{p}\frac{T'_{Pi}}{\sqrt{2}\tau_P} \tag{21}$$

$$\dot{\gamma}_I^{p} = \dot{\gamma}^{o}\exp\left[\frac{-\Delta G}{k_b\theta}\right]\sinh\left[\frac{\Delta G}{k_b\theta}\frac{\tau_P}{s}\right] \tag{22}$$

where $\tau_P = \sqrt{(1/2)(T'_{P1}{}^2 + T'_{P2}{}^2 + T'_{P3}{}^2)}$ is the scalar equivalent shear stress. Since a different stress drives yielding, the nonlinear viscous material parameters associated with the shear resistance s in Model II will differ from those of Model I. s will have an initial increase during yield ($\tilde{s}$), a softening with further plasticity ($\hat{s}$), and an increase with network alignment ($\bar{s}$). As in Model I, the initial shear resistance $\tilde{s}_o$ is taken to increase with $\dot{\gamma}_I^{p}$ until reaching a saturated state during plastic deformation reflecting the distributed nature of yield:

$$\dot{\tilde{s}} = \tilde{h}\left(1 - \frac{\tilde{s}}{\tilde{s}_{sat}}\right)\dot{\gamma}_I^{p} \tag{23}$$

where $\tilde{h}$ controls the rate of approach of $\tilde{s}$ to its saturation value $\tilde{s}_{sat}$. To capture a softening that occurs upon percolation, $\hat{s}_o = 0$, which

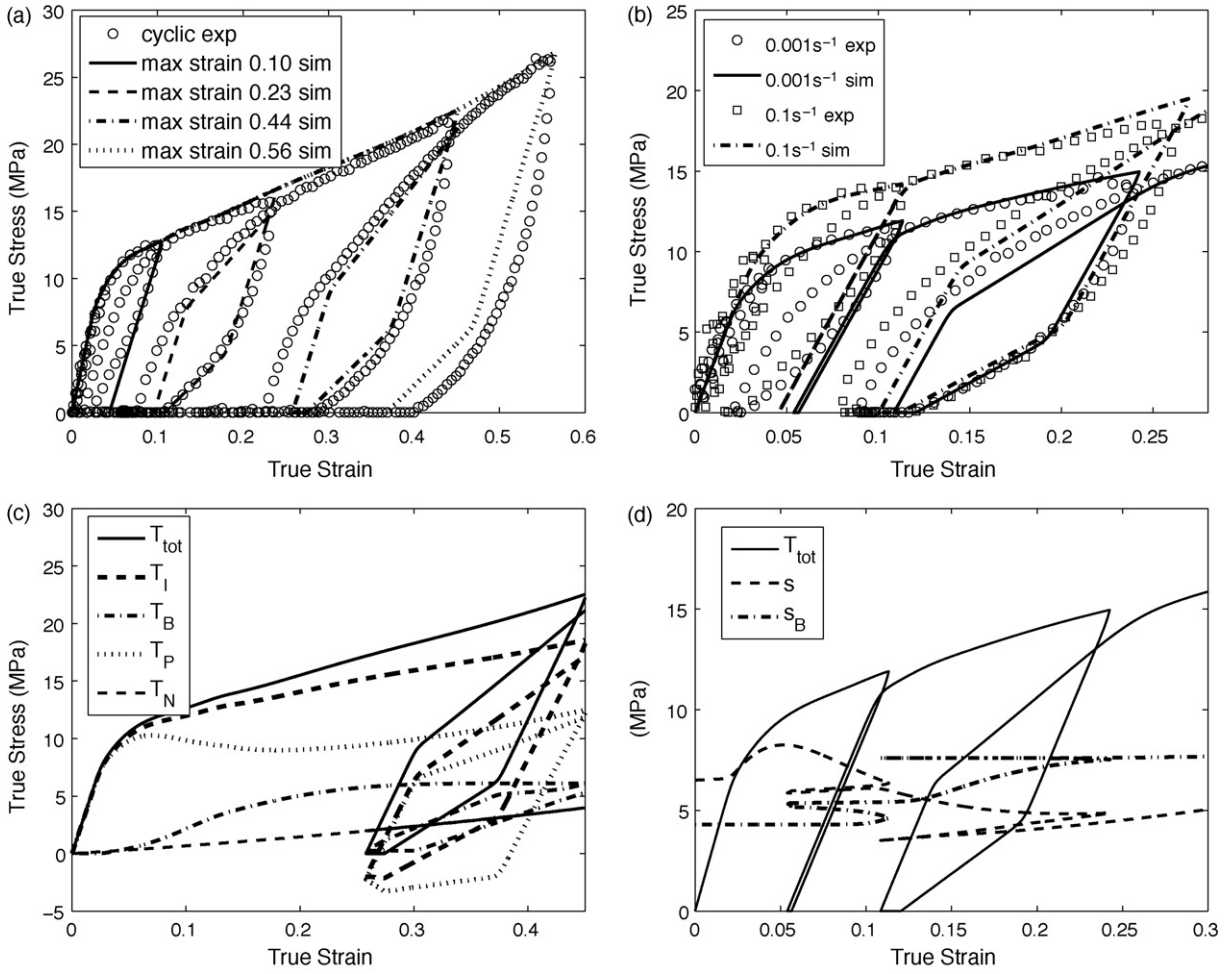

Fig. 13. Model II under tensile cyclic loading at ambient conditions (a) comparison to experimental data at different maximum strain values at a strain rate of 0.01 s^{-1}, (b) comparison to experimental data at different strain rates, (c) contribution of the individual mechanisms to the overall response at 0.01 s^{-1}, and (d) evolution of s and s_B at a strain rate of 0.001 s^{-1}.

is subtracted from $\tilde{s}$, is taken to increase with $\dot{\gamma}_I^p$ at a slower rate than $\tilde{s}$, to its saturated value $\hat{s}_{sat}$:

$$\dot{\hat{s}} = \hat{h}\left(1 - \frac{\hat{s}}{\hat{s}_{sat}}\right)\dot{\gamma}_I^p \tag{24}$$

where $\hat{h}$ controls the rate of approach of $\hat{s}$ from its initial value of 0 to its saturation value $\hat{s}_{sat}$. An evolution of this nature is something that is commonly seen in glassy polymers (e.g. [20]). Molecular alignment provides an additional increase to the intermolecular shear resistance captured by the contribution $\bar{s}$:

$$\bar{s} = \bar{h}(\lambda_{chain}^{\bar{n}} - 1) \tag{25}$$

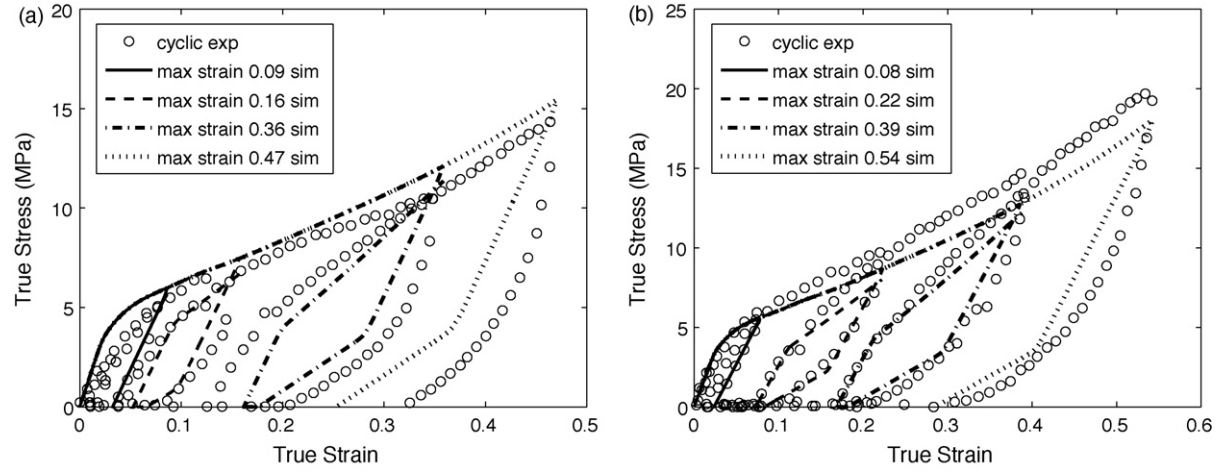

Fig. 14. Model II vs. experiment under tensile cyclic loading at a strain rate of 0.01 s^{-1} (a) at 80 °C and ambient relative humidity (b) in water at 25 °C.

where $\bar{h}$ controls the initial slope and $\bar{n}$ controls the nonlinearity. The shear resistance (s) is then given by:

$$s = \tilde{s} - \hat{s} + \bar{s}. \tag{26}$$

The network mechanism is unchanged by the addition of the back stress to the intermolecular mechanism.

4.2.1. Temperature and hydration dependence features

The existing kinematics and constitutive definitions for the inclusion of the effects of temperature and hydration in Model I are unchanged in Model II. μ and the plasticity dependent portion of the shear resistance to plastic flow $\tilde{s} - \hat{s}$ are multiplied by the reduction factor to obtain $\mu(\theta, \phi)$ and $[\tilde{s} - \hat{s}](\theta, \phi)$, respectively. Additionally the current state values of μ_B and s_B independent of temperature and hydration are multiplied by the reduction factor to obtain $\mu_B(\theta, \phi)$ and $s_B(\theta, \phi)$, respectively.

A method for reducing the additional material parameters required for Model II is provided in Appendix A along with the parameter values.

4.2.2. Results

Model II retains the ability to capture all stress–strain loading features and dependencies captured in Model I. Model II is able to capture the nonlinear unloading and reloading both as a function of strain and as a function of strain rate as shown in Fig. 13a and b. Focusing on the unloading curves, the highly nonlinear unloading behavior is captured as a reverse yield event that occurs during unloading assisted by a back stress. The evolution in the intermolecular stress and the back stress enable yield corners to occur at the appropriate total stress during unloading and reloading for different strains and strain rates (Fig. 13c and d). Model II accurately reproduces both the decrease in yield stress observed during reloading (as captured by the initial yield stress) and the increased post-yield slope until the reloading curve reaches the monotonic curve. These same features are experimentally observed at elevated temperature and hydration and are captured by Model II (Fig. 14). The temperature and hydration reduction factors which work for capturing the effect of temperature and water content on the shear modulus and yield stress are also successful in capturing the effect of temperature and water content on the reverse and reloading yield stresses.

Determination of the material parameters for the Model II is given in Appendix A.

5. Concluding remarks

The mechanical behavior of the Nafion (NRE212), which typically serves as the polymer electrolyte membrane in low temperature fuel cells, has been experimentally characterized as a function of rate, temperature, and hydration for both monotonic and cyclic loading. These experiments provide details on the subtleties of the time, temperature, and hydration dependence as well as new details on the cyclic behavior which are critical to understanding membrane deformation and failure in fuel cell operation. The behavior of NRE212 was found to be transversely isotropic and quantitatively, but not qualitatively, dependent on the chemical pre-treatment. Dynamic mechanical analysis showed that, under dry (30%RH) conditions, the material begins to transition from the glassy to the rubbery state at 75 °C, with a glass transition of 105 °C. DMA further revealed that the fully hydrated state is significantly more compliant than the dry state, with the material beginning to transition from the glassy to the rubbery state at 40 °C. Large strain monotonic tensile tests revealed an initial elastic response followed by a rollover type yield and moderate post-yield strain hardening. The rate-dependent stress–strain behavior was seen to be highly dependent on temperature and hydration: the dry state transitions from an elastic–plastic behavior at 25 ° C to an increasingly rubbery behavior with decreasing elastic modulus and yield stress as temperature is increased through the glass transition to 100 °C. At all temperatures, increasing hydration acts to decrease the elastic stiffness and yield stress. Unloading from different strains revealed the elastic–plastic nature of the behavior even for the elevated temperature and hydrated states. Cyclic loading–unloading–reloading excursions to different strains showed significant nonlinear recovery at all strains past yield with a highly nonlinear reloading behavior which has an apparent reduced yield stress and then rejoins the initial loading path. The significant time, temperature, and hydration dependent mechanical behavior evident from this uniaxial tensile data suggests that the rate of heating/cooling and hydrating/drying the MEA during startup/shutdown of the fuel cell as well as whether these operations are done simultaneously or sequentially will be critical to the nature and magnitude of the stresses that develop in the membrane.

A constitutive model was developed in two stages to capture the mechanical behavior of Nafion NRE212; the first to capture all the key elements of monotonic loading and the second to capture all the key elements of more general loading histories. Model I, consisting of a linear-elastic–plastic intermolecular component and a nonlinear network component, was shown to be capable of capturing the rate, temperature, and hydration dependence of monotonic loading but not the unloading or reloading behavior. The intermolecular resistance captures the local intermolecular barriers to initial elastic deformation and also captures the thermally activated nature of yield; these intermolecular barriers are modeled to decrease with increasing temperature and hydration, in particular mimicking the reduction in these barriers as the material approaches and enters the glass transition regime, successfully capturing the strong temperature and hydration dependence of the stress–strain behavior. Model II, a version of Model I enhanced with the addition of a back stress to the viscoplastic element in the intermolecular component, was shown to additionally be capable of capturing the rate, temperature, and hydration dependence of the cyclic response. The back stress has similar properties to the intermolecular elastic–plastic element, with an initial elastic portion, a rate-dependent saturation, and barriers which decrease in the same way with temperature and hydration. The back stress develops during inelastic deformation and then helps to drive reverse deformation during unloading. This enables the model to capture the highly nonlinear nature of unloading and reloading including the reduction in reloading yield stress which occurs with increasing strain. Impressively, this model captures the temperature and hydration dependence of the cyclic behavior without any additional material parameters. Model II is capable of capturing the behavior of Nafion over the wide range of strains, environmental conditions, and loading conditions relevant to modeling the membrane within the fuel cell. This will enable analysis of the pertinent complex hygrothermal-mechanical loading conditions. The constitutive model has been formulated for use within nonlinear finite element analysis and will be utilized in simulations of the fuel cell stack, including relevant boundary conditions, and subjected to hygrothermal cycling. In particular, these simulations will track the development of tensile in-plane stresses, negative hydrostatic pressures, and cyclic plastic strains as indicators of fatigue failure. A parametric study of this nature will be presented in future work.

Acknowledgements

Funding for this work was provided by an MIT Presidential Fellowship, an MIT Martin Environmental Fellowship, NSF grant CMMI-0700414, and the Masdar Institute.

Appendix A. Determination of material constants

All parameter determination is done with data at a strain rate of 0.01 s^{-1} and at ambient conditions (25 °C, 30%RH) unless otherwise stated.

A.1. Model I

A.1.1. Mechanism I

The Cauchy stress due to the intermolecular component is prescribed by:

$$T_{Ii} = \frac{1}{J^e}[2\mu(\ln \lambda_{Ii}^{e})' + \kappa \ln J^e] \tag{27}$$

Any two elastic constants can define the intermolecular elastic response. The elastic modulus (E) is found from the slope of the initial linear-elastic region of the stress–strain curve. The Poisson's ratio (ν) is estimated from the ratio of horizontal to vertical strain found via the video extensometer in this same region. These two constants are then converted into the required shear (μ) and bulk (κ) moduli via Eqs. (28) and (29), respectively. The dependence of the elastic constants on temperature and hydration will be discussed later:

$$\mu = \frac{E}{2(1+\nu)} \tag{28}$$

$$\kappa = \frac{E}{3(1-2\nu)} \tag{29}$$

The magnitude of the rate of plastic deformation is described by:

$$\dot{\gamma}_I^p = \dot{\gamma}^o \exp\left[-\frac{\Delta G}{k_b\theta}\right] \sinh\left[\frac{\Delta G}{k_b\theta}\frac{\tau_I}{s}\right] \tag{30}$$

$$s = \tilde{s} + \bar{s} \tag{31}$$

The network stress contribution is negligible at yield, so the stress on the plastic component can be approximated by the total stress. Therefore, the three constants ($\dot{\gamma}^o$,ΔG,s) that characterize this rate of plastic deformation are fit to the yield stress as a function of rate and temperature. For fitting purposes it is assumed that only the forward process is active, Eq. (30) can then be rewritten as:

$$\dot{\gamma}_I^p = \dot{\gamma}^o \exp\left[-\frac{\Delta G}{k_b\theta}\right] \exp\left[\frac{\tau\Omega}{k_b\theta}\right] \tag{32}$$

where the Ω is the activation volume related to the other material properties as $\Omega = \Delta G/s$. Eq. (32) can be solved for the uniaxial stress $\sigma = \sqrt{3}\tau$ as a function of the uniaxial strain rate $\dot{\epsilon}$, the temperature θ and the three unknown constants ($\dot{\gamma}^o$,ΔG,Ω). The slope of σ vs. $\ln\dot{\epsilon}$ (Fig. 15a), which equals $\sqrt{3}k_b\theta/\Omega$, gives the value for Ω. The slope of σ vs. θ (Fig. 15b), which equals $\sqrt{3}(k_b/\Omega)\ln(\sqrt{3}\dot{\epsilon}/\dot{\gamma}^o)$, gives the value for $\dot{\gamma}^o$. The y-intercept of σ vs. θ, which equals $\sqrt{3}\Delta G/\Omega$, gives the value for ΔG. The equation is put back in terms of s using $s = \Delta G/\Omega$, where this s is the value of s at the end of the rollover yield and is approximately $\tilde{s}_{sat}$.

The evolution of $\tilde{s}$ is controlled via:

$$\dot{\tilde{s}} = \tilde{h}\left(1 - \frac{\tilde{s}}{\tilde{s}_{sat}}\right)\dot{\gamma}_I^p \tag{33}$$

$\tilde{s}_o$ determines the initial yield condition and is set according to the stress at which the rollover yield starts. $\tilde{s}$ increases according to the shape of the rollover yield to $\tilde{s}_{sat}$. $\tilde{h}$ controls the rate of this evolution to match the shape of the rollover yield. $\bar{s}$ captures the portion of the strain hardening that does not arise from the network component:

$$\bar{s} = \bar{h}(\lambda_{chain}^{\bar{n}} - 1) \tag{34}$$

where $\bar{h}$ controls the initial slope and $\bar{n}$ controls the nonlinearity.

The overall evolution in s as well as the separate contributions of $\tilde{s}$ and $\bar{s}$ are shown in Fig. 16.

A.1.2. Mechanism N

The orientation hardening is described by:

$$T_{Ni} = \frac{\mu_N}{J_N^m \lambda^s} B_{Ni}^{m\prime} \tag{35}$$

The rubbery shear modulus μ_N is fitted to monotonic extension data at 100 ° C for which it is assumed that the intermolecular contribution is minimal.

Thermal and hydration dependence: The bulk modulus is assumed to be independent of temperature and water content. The intermolecular and back stress shear moduli and isotropic plastic deformation resistances are defined as uncoupled functions of temperature and water content as taken from the independent variation in elastic modulus stress with these two factors. Two reduction factors (one each) are calculated independently for the temperature and water content effect from elastic modulus data normalized relative to the modulus at ambient conditions (25 °C, 30%RH). These fits are shown in Fig. 17. In the simulation the product of these two factors give the total reduction factor that is multiplied by μ and $\tilde{s}$ at room temperature and relative humidity

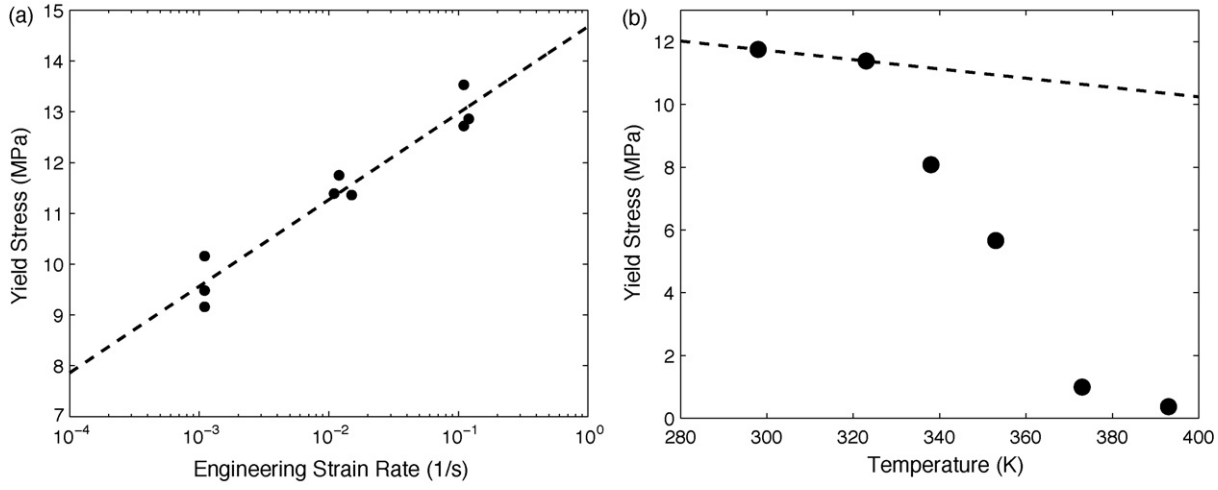

Fig. 15. Data used to fit rate of plastic deformation. (a) Yield stress as a function of engineering strain rate. (b) Yield stress as a function of temperature at an engineering strain rate of 0.01 s^{-1}.

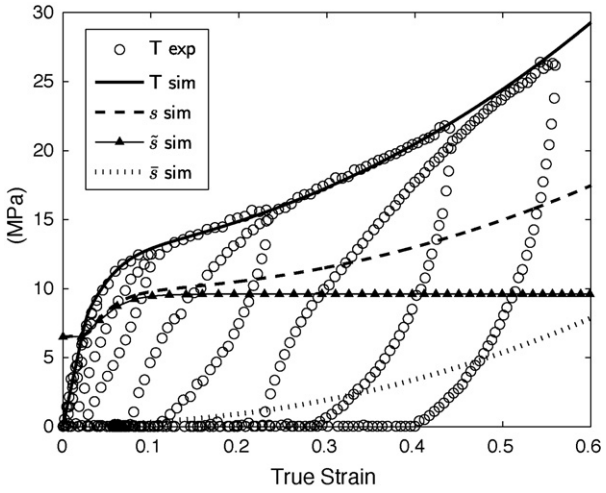

Fig. 16. Evolution of s and its components during monotonic tensile loading for Model I.

to find $\mu(\theta,\phi)$ and $\tilde{s}(\theta,\phi)$, respectively. The reduction factor does not effect evolution of these parameters, it is applied at each step to the current evolved values and is not stored for the following step.

The swelling deformation is prescribed by:

$$\lambda^s = 1 + \beta\Delta\phi + \alpha\Delta\theta \tag{36}$$

The thermal expansion coefficient $\alpha = 1.23e-4/K$ is taken from literature [35]. The hygro expansion coefficient, β, is determined from the relation between water content and linear expansion based on the additive volume assumption. Starting from a completely dehydrated condition the total volume of the membrane can be expressed as:

$$V_{tot} = V_{dry} + V_{water}. \tag{37}$$

where V_{dry} is the volume of the dry membrane and V_{water} is the volume of water added to the membrane. If isotropic swelling is assumed then the stretch associated with this swelling is:

$$\lambda^s = \left(1 + \frac{V_{water}}{V_{dry}}\right)^{\frac{1}{3}} \tag{38}$$

The volume ratio can be written in terms of the molecular weights of the membrane($M_{membrane}$) and water(M_{water}), and the mole ratio of water to sulfonic acid groups as:

$$\lambda^s = \left(1 + \phi\frac{M_{water}}{M_{membrane}}\right)^{\frac{1}{3}} \tag{39}$$

where

$$M_{membrane} = \frac{EW}{\rho_{membrane}} = \frac{1100}{1.906\,\mathrm{g\,cm^{-3}}} = 558.8\,\mathrm{g\,cm^{-3}} \tag{40}$$

$$M_{water} = 18.016\,\mathrm{g\,cm^{-3}} \tag{41}$$

where EW is the equivalent weight of the membrane defined as the weight of the membrane per mole of sulfonic acid group and $\rho_{membrane}$ is the membrane density. Both values are taken from the Dupont specifications sheet associated with NRE212. We chose to use ambient conditions (25 °C, 30%RH) as the reference state. It is estimated from literature that $\phi = 1.5$ at ambient conditions [4,18]. Substituting in numbers we therefore adjust the formula for λ^s such that $\lambda^s = 0$ at $\phi = 1.5$:

$$\lambda^s = \left(\frac{\phi}{31} + 1\right)^{\frac{1}{3}} - 0.016. \tag{42}$$

To find ϕ as a function of λ^s we invert this equation:

$$\phi = 31[(\lambda^s + 0.016)^3 - 1]. \tag{43}$$

The hygro expansion coefficient, defined as $\beta = (\partial \ln\lambda^s/\partial\phi)$ is then equal to

$$\beta = \frac{1}{93}\frac{1}{\left((\phi/31)+1\right)^{1/3} - 0.016}\left(\frac{\phi}{31}+1\right)^{-\frac{2}{3}} \tag{44}$$

For simplicity we chose to estimate β as independent of ϕ and take for it the mean value for a range of ϕ from 1.5 to 22.

The parameters used in the Model I are listed in Table 1.

A.2. Model II

In order to fit the enhanced version of the model (Model II) parameters are required for the evolution of μ, the revised evolution of s, and the back stress. All other parameters will remain the same.

A.2.1. Mechanism I

The evolution of μ from its initial value μ_o to a minimum value through yield is governed by:

$$\dot{\mu} = h\left(1 - \frac{\mu}{\mu_{sat}}\right)\dot{\gamma}_I^p \tag{45}$$

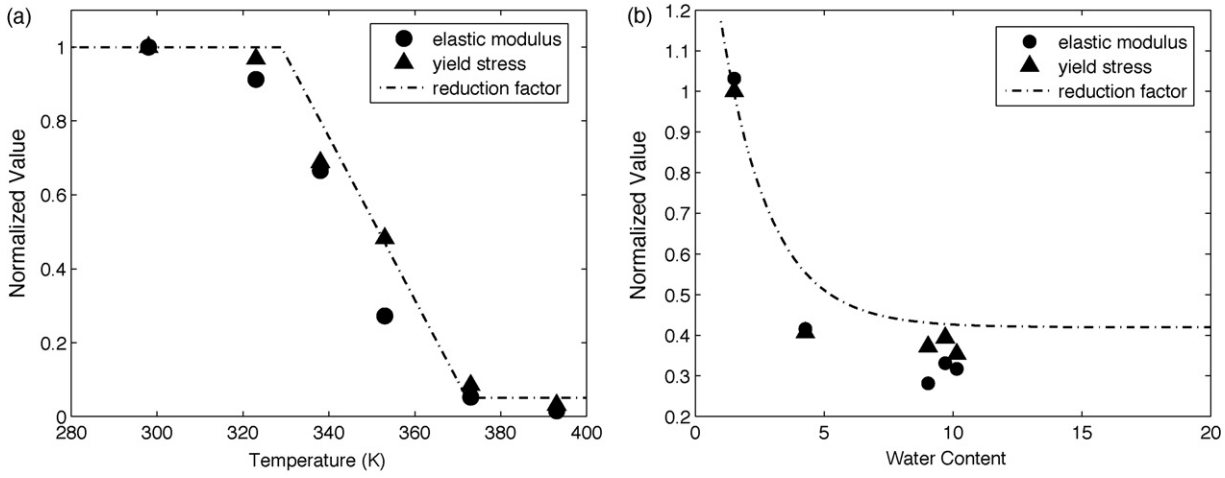

Fig. 17. Shear modulus adjustment factor fit to normalized elastic modulus and yield stress data for (a) temperature and (b) water content.

Table 1
Material parameters for Model I.

Model component	Material parameter	Value
Elastic	κ	3.3×10^8 Pa
	μ	1.1×10^8 Pa
Rate-dependent yield	$\dot{\gamma}^o$	$6.72\,s^{-1}$
	ΔG	8.98×10^{-20} J
	$\tilde{s}_o$	6.5×10^6 Pa
Distributed yield	$\tilde{h}$	4×10^8 Pa
	$\tilde{s}_{sat}$	9.6×10^6 Pa
Isotropic hardening	$\bar{h}$	3.6×10^7 Pa
	$\bar{n}$	1
Network	μ_N	3.3×10^6 Pa
Thermal expansion	α_θ	$1.23 \times 10^{-4}\,K^{-1}$
Hygro expansion	β_ϕ	$8.1 \times 10^{-3}\,\phi^{-1}$

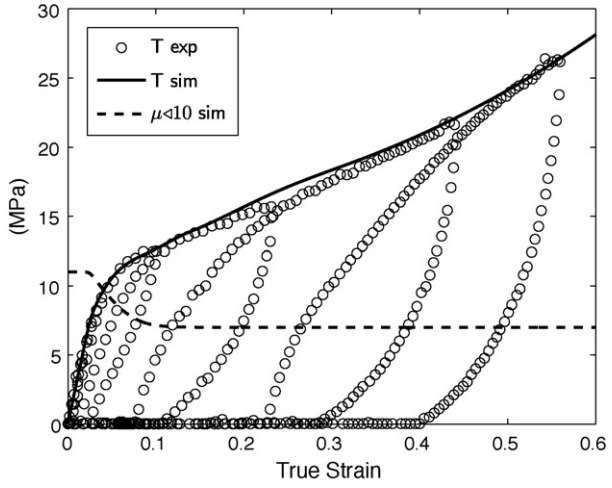

Fig. 18. Evolution of μ during monotonic tensile loading for Model II.

where μ_{sat} is set to the unloading slope of a cycle to a peak strain of 0.1 (just past yield) and h is set such that that minimum value has been nearly reached by that strain (Fig. 18). A cycle to a strain of this value has been chosen because this slope is found to be smaller than the unloading and reloading slopes of cycles at smaller strains and consistent with the unloading and reloading slopes of cycles at larger strains when the network contribution is accounted for.

The elastic portion of the back stress is prescribed by:

$$T'_{Bi} = \frac{1}{J} 2\mu_B \ln \lambda_{Bi} \tag{46}$$

μ_B is set according to the slope as the stress approaches zero during unloading of a cycle to a peak strain of 0.23. In this region the back stress dominates the stress–strain behavior; the intermolecular contribution to the slope is negligible because it has yielded, s is not evolving strongly, and the network contribution to the slope is negligible because the strain is still relatively small.

The magnitude of the rate of plastic deformation is described by:

$$\dot{\gamma}_I^p = \dot{\gamma}^o \exp\left[-\frac{\Delta G}{k_b\theta}\right] \sinh\left[\frac{\Delta G}{k_b\theta}\frac{\tau_P}{s}\right] \tag{47}$$

$$s = \tilde{s} - \hat{s} + \bar{s} \tag{48}$$

Both the back stress and the network stress contributions are negligible at yield, so the stress on the plastic component can be approximated by the total stress. $\dot{\gamma}^o$, ΔG, and s at the end of the rollover yield are therefore unchanged from Model I.

The evolution of $\tilde{s}$ is controlled via:

$$\dot{\tilde{s}} = \tilde{h}\left(1 - \frac{\tilde{s}}{\tilde{s}_{sat}}\right)\dot{\gamma}_I^p \tag{49}$$

$\tilde{s}_o$ sets the initial yield condition and is set according to the stress at which the rollover yield starts. $\tilde{s}$ increases according to the shape of the rollover yield with $\tilde{s}_{sat}$ equal to the s value at the end of the yield rollover. $\tilde{h}$ controls the rate of this evolution to match the shape of the rollover and will differ somewhat from $\tilde{h}$ in Model I because of the simultaneous evolution of μ and $\hat{s}$. The evolution of the $\hat{s}$ and $\bar{s}$ components of s are given below. They are intricately tied with the evolution of s_B and the back stress and determination of the associated parameters will be discussed shortly:

$$\dot{\hat{s}} = \hat{h}\left(1 - \frac{\hat{s}}{\hat{s}_{sat}}\right)\dot{\gamma}_I^p \tag{50}$$

$$\bar{s} = \bar{h}(\lambda_{chain}^{\bar{n}} - 1) \tag{51}$$

The magnitude of the rate of plastic back stress deformation is described by:

$$\dot{\gamma}_B^p = \dot{\gamma}^o \exp\left[-\frac{\Delta G}{k_b\theta}\right] \sinh\left[\frac{\Delta G}{k_b\theta}\frac{\tau_B}{s_B}\right] \tag{52}$$

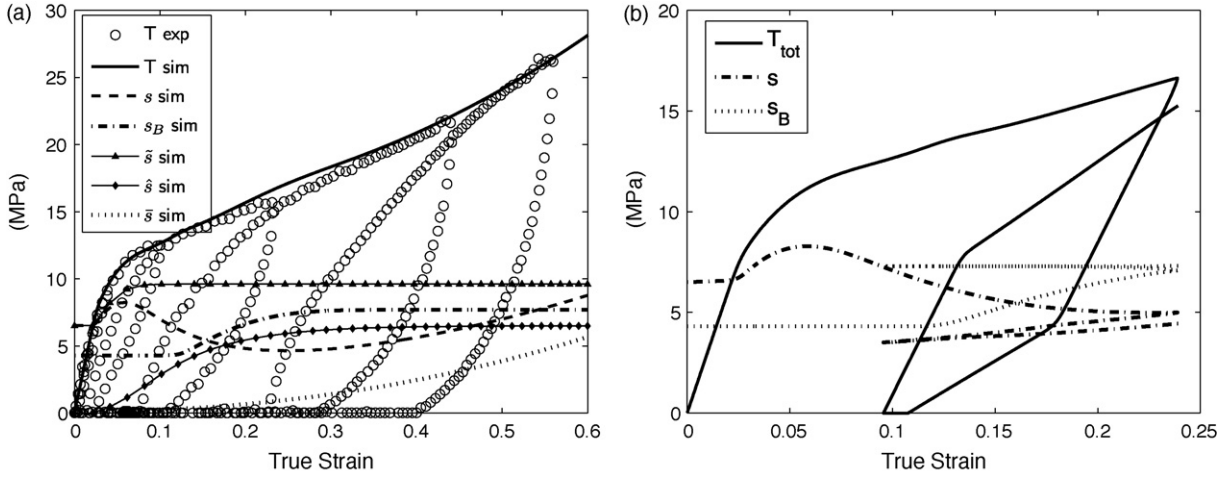

Fig. 19. Evolution of s and its components and s_B in Model II (a) during monotonic tensile loading and (b) during cyclic loading.

Table 2
Material parameters for Model II.

Model component	Material parameter	Value
Elastic	κ	3.3×10^8 Pa
	μ_o	1.1×10^8 Pa
Elastic evolution	h	4.7×10^9 Pa
	μ_{sat}	7.0×10^7 Pa
Rate-dependent yield	$\dot{\gamma}^o$	$6.72\,s^{-1}$
	ΔG	8.98×10^{-20} J
	$\tilde{s}_o$	6.5×10^6 Pa
Distributed yield	$\tilde{h}$	1.2×10^9 Pa
	$\tilde{s}_{sat}$	9.6×10^6 Pa
	$\hat{h}$	7.5×10^7 Pa
	$\hat{s}_{sat}$	6.5×10^6 Pa
Isotropic hardening	$\bar{h}$	2.6×10^7 Pa
	$\bar{n}$	1
Back stress	μ_B	2.65×10^7 Pa
	s_{Bo}	4.3×10^6 Pa
	h_B	2.3×10^8 Pa
	s_{Bsat}	7.7×10^6 Pa
Network	μ_N	3.3×10^6 Pa
Thermal expansion	α_θ	$1.23 \times 10^{-4}\,K^{-1}$
Hygro expansion	β_ϕ	$8.1 \times 10^{-3}\,\phi^{-1}$

$\dot{\gamma}^o$ and ΔG are the same as for the intermolecular plastic deformation. The evolution of s_B is governed by:

$$\dot{s}_B = h_B \left(1 - \frac{s_B}{s_{Bsat}}\right) \dot{\gamma}_B^p \tag{53}$$

s and s_B work in conjunction to set the unloading and reloading corners at the appropriate stress levels. However, since s has a direct effect on the intermolecular stress and s_B has an indirect effect on the intermolecular stress, each has a strong influence on the shape of the loading curve as well. $\hat{h}$, $\bar{h}$, h_B, $\hat{s}_{sat}$, s_{Bsat}, and $\bar{n}$ are simultaneously fit to the cyclic data. In general $\hat{s}_{sat}$ and s_{Bsat} are responsible for setting the unloading yield for small to moderate strains (< 0.3); $\bar{h}$ and $\bar{n}$ are responsible for setting the unloading yield for moderate to large strains (> 0.3); and $\hat{h}$, h_B, and the initial value of s_B provide a smooth loading curve. The overall evolutions in s and s_B as well as those of the individual components $\tilde{s}$, $\hat{s}$, and $\bar{s}$ are shown in Fig. 19.

The temperature and hydration reduction factor which is used to calculate $\mu(\theta, \phi)$, $[\tilde{s} - \hat{s}](\theta, \phi)$, $\mu_B(\theta, \phi)$ and $s_B(\theta, \phi)$ from μ, $\tilde{s} - \hat{s}$, μ_B, and s_B is unchanged from that used in Model I.

The parameters used in Model II are listed in Table 2.

References

[1] S. Kundu, L.C. Simon, M. Fowler, S. Grot, Polymer 46 (2005) 11707–11715.
[2] Y. Tang, A.M. Karlsson, M.H. Santare, M. Gilbert, S. Cleghorn, W.B. Johnson, Materials Science and Engineering A 45 (2006) 297–304.
[3] M.B. Satterfield, P.W. Majsztrik, H. Ota, J.B. Benziger, A.B. Bocarsly, Journal of Polymer Science Part B: Polymer Physics 44 (2006) 2327–2345.
[4] P.W. Majsztrik, A.B. Bocarsly, J.B. Benziger, Macromolecules 41 (2008) 9849–9862.
[5] M.B. Satterfield, J.B. Benziger, Journal of Polymer Science Part B: Polymer Physics 47 (2009) 11–24.
[6] D. Liu, S. Kyriakides, S.W. Case, J.J. Lesko, Y. Li, J. McGrath, Journal of Polymer Science Part B: Polymer Physics 44 (2006) 1453–1465.
[7] D. Liu, M.A. Hickner, S.W. Case, J.J. Lesko, Journal of Engineering Materials and Technology 128 (2006) 503–508.
[8] A. Kusoglu, Y. Tang, M. Lugo, A.M. Karlsson, M.H. Santare, S. Cleghorn, W.B. Johnson, Journal of Power Sources 195 (2010) 483–492.
[9] A.Z. Weber, J. Newman, American Institute of Chemical Engineers Journal 50 (2004) 3215–3226.
[10] A. Kusoglu, A.M. Karlsson, M.H. Santare, S. Cleghorn, W.B. Johnson, Journal of Power Sources 161 (2006) 987–996.
[11] A. Kusoglu, Y. Tang, M.H. Santare, A.M. Karlsson, S. Cleghorn, W.B. Johnson, Journal of Fuel Cell Science and Technology (2009) 6.
[12] R. Solasi, Y. Zou, X. Huang, Mechanics of Time-Dependent Materials 12 (2008) 15–30.
[13] Y. Lai, C.K. Mittlesteadt, C.S. Gittleman, D.A. Dillard, Journal of Fuel Cell Science and Technology 6 (2009), 021002–1-13.
[14] L.G. Hector, Y. Lai, W. Tong, M.J. Lukitsch, Journal of Fuel Cell Science and Technology 4 (2007) 19–28.
[15] M.N. Silberstein, Mechanics of Proton Exchange Membranes: Time, Temperature, and Hydration Dependence of the Stress–Strain Behavior of Persulfonated Polytetrafluoroethylene, MS Thesis, Massachusetts Institute of Technology, Cambridge, MA, February 2008.
[16] G. Gebel, P. Aldebert, M. Pineri, Polymer 34 (1993) 333–339.
[17] D.R. Morris, X.J. Sun, Journal of Applied Polymer Science 50 (1993) 1445–1452.
[18] S. Yeo, A. Eisenberg, Journal of Applied Polymer Science 21 (1977) 875–898.
[19] O.A. Hasan, M.C. Boyce, Polymer 34 (1993) 5085–5092.
[20] O.A. Hasan, M.C. Boyce, Polymer and Engineering Science 35 (1995) 331–344.
[21] M.C. Boyce, D.M. Parks, A.S. Argon, Mechanics of Materials 7 (1988) 15–33.
[22] E.M. Arruda, M.C. Boyce, International Journal of Plasticity 9 (1993) 697–720.
[23] E.M. Arruda, M.C. Boyce, R. Jayachandran, Mechanics of Materials 19 (1995) 193–212.
[24] J.S. Bergstrom, M.C. Boyce, Journal of Mechanics and Physics of Solids 46 (1998) 931–954.
[25] M.C. Boyce, S. Socrate, P.G. Llana, Polymer 41 (2000) 2183–2201.
[26] A.D. Mulliken, M.C. Boyce, International Journal of Solids and Structures 43 (2006) 1331–1356.
[27] R.B. Dupaix, M.C. Boyce, Mechanics of Materials 39 (2007) 39–52.
[28] C.P. Buckley, D.C. Jones, Polymer 36 (1995) 3301–3312.
[29] J.S. Bergstrom, L.B. Hilbert, Mechanics of Materials 37 (2005) 899–913.
[30] L. Anand, N.M. Ames, V. Srivastava, S.A. Chester, International Journal of Plasticity 25 (2009) 1474–1494.
[31] N.M. Ames, V. Srivastava, S.A. Chester, L. Anand, International Journal of Plasticity 25 (2009) 1495–1539.
[32] P.J. Flory, J. Rehner, Journal of Chemical Physics 11 (1943) 521–526.
[33] M.C. Boyce, E.M. Arruda, Mathematics and Mechanics of Solids 6 (2001) 641–659.
[34] O.B. Salamantina, S.N. Rudnev, V.V. Voenniy, E.F. Oleynik, Journal of Thermal Analysis 38 (1992) 1271–1281.
[35] Product Information, DuPont Nafion PFSA Membranes, 2004.